A Smartphone-Based Laser Measuring System for Gap and Flush Assessment in Car Body

Long Hoang Pham ⓘ, Duong Nguyen-Ngoc Tran ⓘ, Jin Young Byun ⓘ, Chul Hong Rhie ⓘ, and Jae Wook Jeon ⓘ, *Senior Member, IEEE*

***Abstract*—This article presents a portable smartphone-based laser measurement system (SLM) for measuring gaps and flushes on a car body. The system is designed to replace conventional gauges that are used by human operators. The developed device consists of a smartphone and an off-the-shelf laser-line projector held together by a three-dimensional–printed structure. It captures images of a laser line scattered on target surfaces, identifies the extreme points on the laser profiles, and obtains gap and flush measurements with minimal uncertainty. Since the smartphone is used as the operational unit, the measurement data can be stored and allows the capability for data transfer with other storage locations. Experiments were performed on the specimens and real cars to validate the application of the developed system. The measurement uncertainty on a real car was reported as ±0.201 mm for gap and ±0.154 mm for flush.**

***Index Terms*—Displacement measurement, image processing, instrumentation and measurement, smartphone.**

Fig. 1. Prototype of the SLM device using an Apple iPhone X.

I. INTRODUCTION

THE inspection of gap and flush (G&F) between two surfaces on a car body is an ongoing research problem in automobile manufacturing. The gap is the horizontal separation between two surfaces, and the flush is the vertical displacement between two surfaces in the orthogonal direction. As stated in [1], defects resulting from large G&F between the car body and various panels (doors, hood, and others) can create unpleasant noises, poor insulation, or water leakage, which reduce the car's quality and performance over time. Hence, identifying defects during the assembly process is crucial to prevent further failure propagation to downstream processes.

Automation level of the assembly process enables G&F to be measured autonomously in dedicated areas, exploiting stationary measurement systems as in [2]–[4]. These systems have the advantage of speed, and complete electronic circuitry makes the sensors respond quick enough to be used easily on a high-speed production line. The only drawback of these systems is their high cost, which hinders their use throughout the whole assembly process. Thus, in some areas, operators still take G&F measurements using feeler gauges and dial gauges. However, the latter approach is subject to high human error and is time-consuming. Additionally, no data are recorded during the inspection, resulting in higher labor costs to store the measurement results digitally.

The need to develop new instrumentation as a replacement for conventional manual gauges is of great importance. One attempt was made to adopt a portable stereo camera system for handheld use [5]. However, the system requires placing fiducial markers on the measuring targets to act as the feature points, which is inconvenient. Pribanic *et al.* [6] turned smartphones into 3-D reconstruction devices based on the infrared projection of a pseudorandom dots (speckle) pattern and structured light scanning. However, this system was built specifically for the Samsung Galaxy Beam (which includes a camera and an embedded Pico projector), which is no longer produced. Meanwhile, portable laser triangulation-based devices have been on the rise in the market, such as GapGun Pro [7], LMI LaserGauge [8], and In-sight Laser Profiler [9]. Unfortunately, these devices are too expensive to be used widely in low-cost applications. In the literature, researchers have been trying to develop more accessible devices. Slossberg and Kimmel [10] developed a 3-D

Long Hoang Pham, Duong Nguyen-Ngoc Tran, Jin Young Byun, and Jae Wook Jeon are with the Department of Electrical and Computer Engineering, Sungkyunkwan University, Suwon 16419, South Korea (e-mail: phlong@skku.edu; duongtran.k10@gmail.com; jinya@skku.edu; jwjeon@yurim.skku.ac.kr).

Chul Hong Rhie is with the Advanced Manufacturing CAE Team, Hyundai Motor Company, Seoul 03143, South Korea (e-mail: 2fered@hyundai.com).
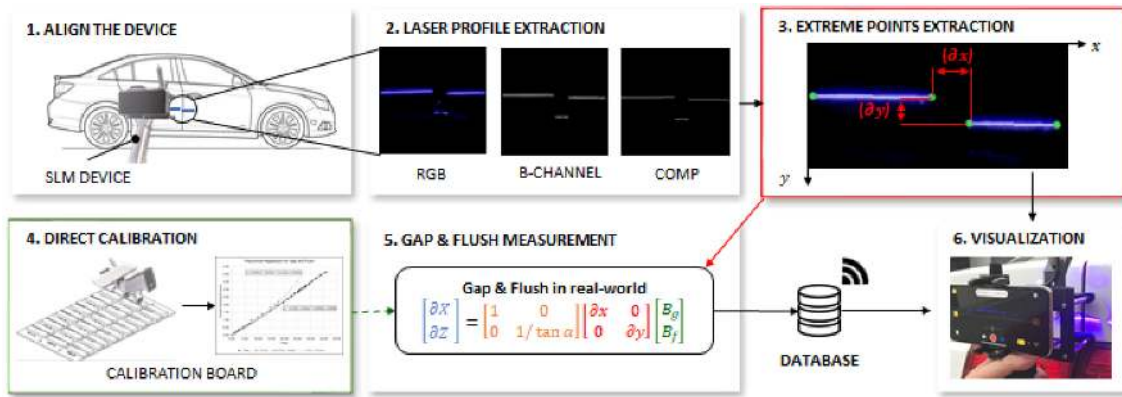
Fig. 2.   Overview of the workflow of the SLM system.

scanner using a smartphone and an inexpensive laser pointer. The drawback of this system is that additional fiducial markers must be placed beside the scanned objects to perform a 3-D reconstruction of the observed objects based on a point cloud. The fiducial marker with known dimension provides the conversion from the pixel measurement to the standard measurement unit. In the GO0D MAN project [11], the authors developed a smartphone-based G&F measurement system [12], equipped with a series of sensors including a Raspberry Pi Zero, a PiCam camera, a time-of-flight (ToF) laser module, and a 405-nm laser line projector. In this system, the Raspberry Pi manages data acquisition and processing, while the smartphone acts as the middleware for exchange of data with the production line and powers the whole system. However, the extra hardware components increase the overall cost of the device.

Inspired by [12], this work presents a novel smartphone-based laser measuring (SLM) device to measure G&F on a car body. The main contributions are as follows.

1) The SLM system consists of only a smartphone and a laser line projector. The device uses the smartphone as the image acquisition, processing, and communication unit. Hence, no additional hardware or sensors are needed.

2) Measurement software is developed consisting of laser profile extraction applying a center of mass peak (CoMP) detection algorithm, localization of extreme points based on a circle fitting algorithm, and a direct calibration method using polynomial fitting with known G&F dimensions to translate pixel measurements to real-world values.

3) Finally, a working prototype of the SLM device has been developed. Experiments were conducted to verify the effectiveness of the proposed approach relative to manual inspection.

The novelty of the proposed approach lies in the use of only a smartphone camera to identify and measure G&F in real time. Moreover, we developed efficient image processing algorithms that can utilize smartphone capabilities. This introduces an improvement over previous methods where additional sensors were necessary. To the best of our knowledge, previous studies have not followed a similar approach for G&F measurement.

TABLE I
MEASURING TARGET SPECIFICATION

Characteristics	Specification	Tolerance
Gap	2.0-4.0 mm	0.2 mm
Flush	0.0-2.0 mm	0.2 mm
Surface material	Aluminum (coated)	
Surface color	Black, white	

TABLE II
HARDWARE COMPONENTS

Component	Characteristics
Camera	12-megapixel CMOS sensor, physical sensor size 4.8×3.6 mm, image resolution 4032×3024, frame rate 60 fps
Lens	focal length 4.25, numerical aperture $N = f/1.8$, shutter speed $t = 1/12000$-$1/4$ s, ISO $S = 22$-2112, $\theta_C = 65.6°$
Laser	Laser diode generator, $\lambda = 405$ nm (violet-blue), 20 mW, input voltage 3-5 V, class II
Optic Pattern	Laser line generator with Gaussian profile, fan angle $\theta_L = 30°$
Triangulation Setup	baseline $b = 65$ mm, triangulation angle $\alpha = 45°$, stand-off distance 110 mm, depth sensing range $\Delta Z = 143.3$ mm, horizontal sensing range $\Delta X = 68.1$ mm

The rest of the article is organized as follows. Section II discusses the hardware design. Section III explains the SLM software in detail. Section IV gives an exhaustive analysis of the experimental results. Finally, Section V concludes this article.

II. HARDWARE DESIGN AND CHARACTERISTICS

A. Measuring Target Specification

The design starting point of the SLM device should be the definition of the measuring target specifications. The gap points between the car body and doors are considered. The parts are made of aluminum painted in black or white. The characteristics of the targets to be measured and the required tolerances are shown in Table I. Because our system leverages several off-the-shelf components, our design must consider the properties of each component that together address several challenges. Hardware characteristics are summarized in Table II.

B. Laser Speckle Effect

The laser speckle effect on different surfaces of different materials (e.g., translucent, transparent, and reflective) is a well-known issue that causes variations in the intensity of the laser line in the image. This is because waves of laser light reflected from different parts of the target surface impinge on the sensor with different phases, causing different optical paths. One possible solution is to use a laser with short wavelength. The SLM device uses a laser of 405-nm wavelength (violet-blue) since it has been demonstrated to provide the best results on all surfaces of the car body [12], [13]. The laser projector is a 20 mW type and can be powered by 5 V batteries.

C. Phone Processor Performance

Fig. 4 shows the per-frame total processing time of the SLM software versus image resolution. Running at a full camera frame rate of 60 f/s allows 16.66 ms to process each frame. We also notice a spike in CPU usage from 67% (at 1280×720 resolution) to 135% (at 1920×1080 resolution). This means that the CPU was overclocked during processing of a higher-resolution image, which significantly increases power consumption and temperature, and can damage the device over extended usage. Therefore, we capture images at 1280×720, which optimizes computational cost and CPU usage within the limits of the smartphone's computing performance.

D. Camera Sensor

This study uses an Apple iPhone X with 12-megapixel wide-angle CMOS (Complementary Metal Oxide Semiconductor) sensor (rear camera) that has a focal length of 4.25 mm and physical sensor dimensions of 4.8×3.6 mm. It has a fixed aperture of $f/1.8$, shutter speed range of $t = 1/12\,000$–$1/4$ s, and sensitivity (ISO value) range of $S = 22$–2112.

E. Reverse Geometry Triangulation

Fig. 3(a) shows the reverse geometry of triangulation, which consists of a laser projector and camera separated by a baseline distance $b = 65$ mm. A laser line is projected onto the target surface at an angle $\alpha = 45°$ while a camera detects scattered light, facing perpendicular to the surface. An image of the laser line is, therefore, captured by the camera, from which the laser profile $Z(X)$ can be computed through trigonometric relations. G&F are then extracted by processing the $Z(X)$ profile. The advantage of this setup is that any small change in the object height produces a large shift in the laser line position, making it better for measuring small differences in flush. The depth sensing range ΔZ is shown in Fig. 3(b) and can be calculated as

$$Z_{\min} = \frac{b \cos \alpha \cos \frac{\theta}{2}}{\cos(\alpha - \frac{\theta}{2})}; Z_{\max} = \frac{b \cos \alpha \cos \frac{\theta}{2}}{\cos(\alpha + \frac{\theta}{2})}$$

$$\Delta Z = Z_{\max} - Z_{\min} \tag{1}$$

which gives $Z_{\min} = 39.5$ mm, $Z_{\max} = 182.8$ mm, and $\Delta Z = 143.3$ mm. The horizontal sensing range ΔX at a distance Z
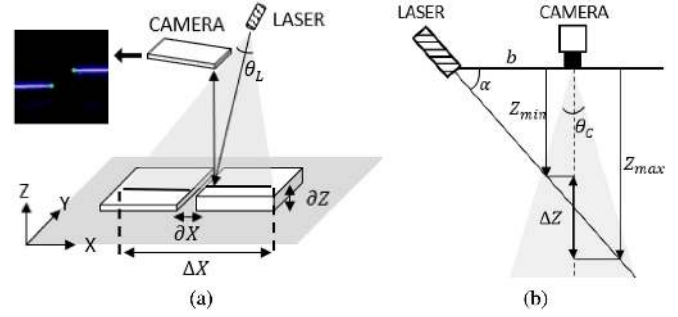

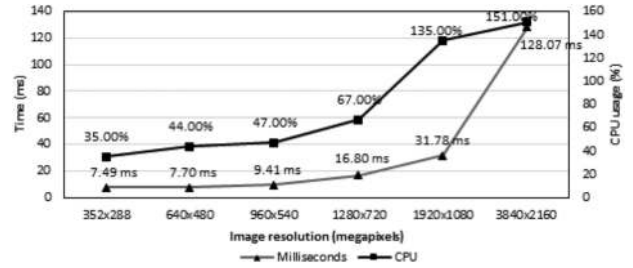Fig. 3. (a) Reverse geometry triangulation setup. (b) Sensing range.

Fig. 4. Total processing timer per frame and CPU usage by our image processing kernel versus image resolution.

depends on the laser optic fan angle θ_L

$$\Delta X = 2\sqrt{b^2 + Z^2} \tan \frac{\theta_L}{2} \tag{2}$$

where the stand-off distance is $Z = 110$ mm, $\Delta X = 68.1$ mm. The sensing ranges ΔZ and ΔX satisfy the measuring characteristics mentioned in Table I.

F. 3-D Structure

Fig. 1 shows the actual prototype SLM device developed for this study. A custom 3-D–printed structure is made to satisfy the triangulation setup specified in Table II. It also includes removable stand-off supports of 110 mm length. The structure's handle also includes batteries to power the laser projector.

III. SLM SOFTWARE

A. Architecture

Fig. 2 describes the workflow of the SLM system for the G&F assessment on a car body. The operator first locates the device on the measuring target. The operator then presses the measure button, and images are captured and processed. The SLM software applies the CoMP detection method to extract two laser profiles at the subpixel level. The extreme points from each profile are extracted. The G&F measurement algorithm estimates the pixel dimensions between the two innermost extreme points. Finally, polynomial regression is used to convert the measured pixel dimensions to standard units (e.g., cm, mm). The measurement results and the laser extraction are visualized on the smartphone screen to provide visual feedback to the operator. A database is used to record a history of all of the previous measurements.
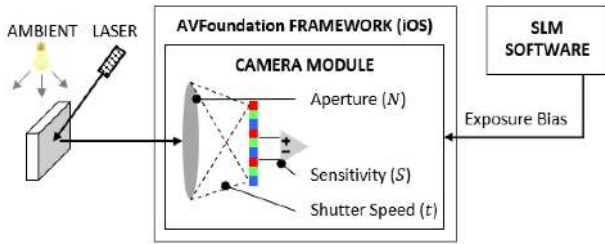
Fig. 5. Block diagram of hardware and software components.

B. Ambient Light Rejection

Our SLM system is an indoor laser measuring device; however, the laser line can be corrupted by ambient light (ceiling lights). In this study, we use a temporal filtering technique to reject ambient light interference. By adapting a shorter camera exposure time, only the laser light is retained in the image [14]. For a digital camera, the exposure time is governed by

$$\text{brightness} \propto N \times t \times S \tag{3}$$

where the aperture value N indicates the size of the opening in the lens to capture the light, which is a fixed value on a smartphone camera. The shutter speed, t, sets the amount of time the sensor is exposed to the light. The faster the shutter speed, the darker the image will be. The ISO sensitivity, S, controls the light absorption rate of the sensor. Reducing this value by half means that double the amount of light is required to produce the same image brightness. Hence, a low ISO value results in darker images and less noise. At a short stand-off distance, a laser pulsing at 20 mW, and a shorter camera exposure help to overcome ambient light interference.

Instead of manually manipulating ISO and shutter speed, the SLM software adjusts the exposure bias value. The exposure bias is a high-level API provided by the smartphone operating system (AVFoundation framework in iOS) to automatically adjusts the ISO and shutter speed to achieve the desired brightness in the image, as shown in Fig. 5. The SLM software subsequently decreases the exposure bias (0.0 by default) until a thin laser line appears in the image, such that the per-column pixel intensity forms a sharp Gaussian distribution, as shown in Fig. 7(a). When the width of the laser line is smaller than a threshold (21 in our experiments), the adjustment process is completed. Fig. 6 shows that an exposure bias value of -3.0 produces the best results in both white and black colors. This algorithm provides good rejection of indoor ambient noise as well as localizing the laser line peak in the image for later steps.

C. Laser Profile Extraction

The laser profile extraction algorithm comprises of image processing operations aimed at precisely locating the subpixel position of the laser peaks in the image.

First, the blue channel is extracted from the RGB image obtained from the camera, since the laser is operating in the violet-blue region. Fig. 7(a) represents the blue channel with the grayscale value for the pixel at the ith row and jth column, denoted by $I(i, j)$. The image at this stage contains salt-and-pepper

noise. Median filtering is a low-cost and effective smoothing technique to remove noise while preserving edges [15]. The median filter works by moving a window through the image, pixel by pixel, replacing each value with the median value. The larger the window size, the stronger the smoothing effect. Fig. 7(b) illustrates the effect of using three common window sizes (3×3, 5×5, and 7×7). We see that the 3×3 median filter has the best result visually. To quantitatively evaluate the filtered images, peak signal-to-noise ratio (PSNR) and structural similarity (SSIM) metrics are used [16]. Since higher PSNR and SSIM values denote better image quality, the median filter with a 3×3 window size is chosen.

Second, the CoMP technique [17] is implemented to extract the center position of the laser line per column at subpixel accuracy. The location of the peak intensity in each column j can be computed by

$$\text{comp}_j = i \times \sum_{i=L}^{U} I(i, j) \bigg/ \sum_{i=L}^{U} I(i, j) \tag{4}$$

where the lower boundary L and the upper boundary U determine the scanning interval and are calculated by

$$L_j = I(\max, j) - 0.5 \text{ s}; U_j = I(\max, j) + 0.5 \text{ s}. \tag{5}$$

The scanning interval varies for each column depending on the row index of the peak value

$$I(\max, j) = \underset{i}{\text{argmax}}(I(i, j)). \tag{6}$$

The value of s controls the scanning interval conforming to the Gaussian distribution of the laser intensity, which ranges from several pixels to tens of pixels. From the experiments, $s = 21$ is chosen to accommodate the spread of the laser line. Examples of the CoMP extraction are shown in Fig. 8.

Third, the resulting comp_j in each column is connected to its neighbors to form the subpixel laser line. Suzuki and Abe's border following algorithm [18] is applied to the CoMP image to produce a set of contours. In Fig. 8, the laser line is broken into three line segments, where the two left-right segments are retained, and the rest are discarded using the following selection criteria:

$$\underset{i,j}{\text{argmax}}\,(lh(Ct_i, Ct_j))$$
$$:= \{Ct_i, Ct_j \in \mathbf{Ct} : \max\,(lh(Ct_i) + lh(Ct_j))\} \tag{7}$$

where $\mathbf{Ct}$ is the set of all extracted contours and $lh(\bullet)$ is the length calculation function applied on each contour. The results are a pair of left (Ct_L) and right (Ct_R) contours.

D. Extreme Point Localization

Two different methods are used to localize the extreme points in the Ct_L and Ct_R contours. On a straight edge gap, the two-point method is commonly used, in which a beginning point and an ending point are selected from each laser line. For the left contour, the ending point L_2 is selected, while in the right contour, the beginning point R_1 is selected. These points are
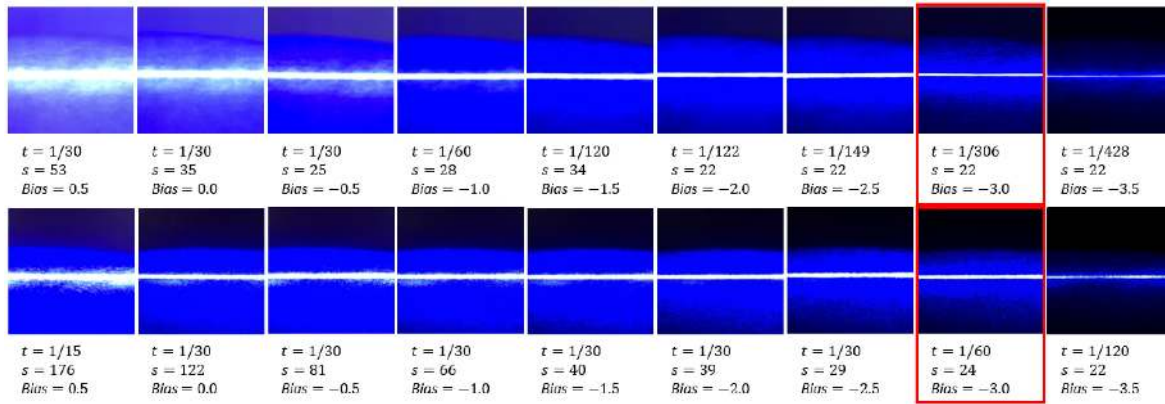
Fig. 6. Illustration the effect of different exposure settings on 405 nm laser light. First row: testing on white surface. Second row: testing on black surface. The best setting is marked in red (best view in color).
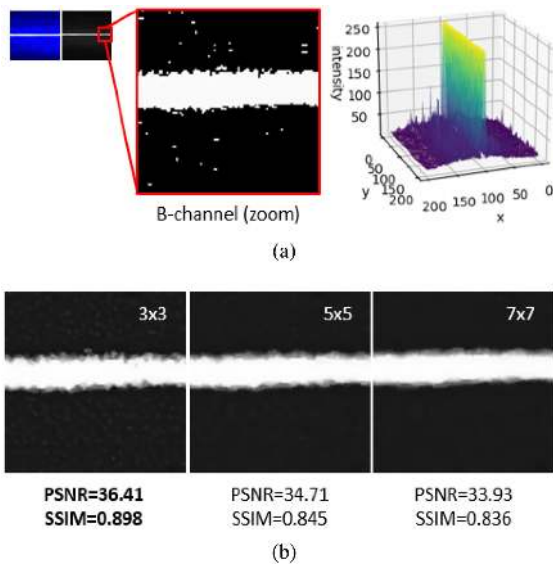

Fig. 7. (a) Visualizing the Gaussian profiles of the 405-nm laser line. (b) Median filter results using different window sizes.
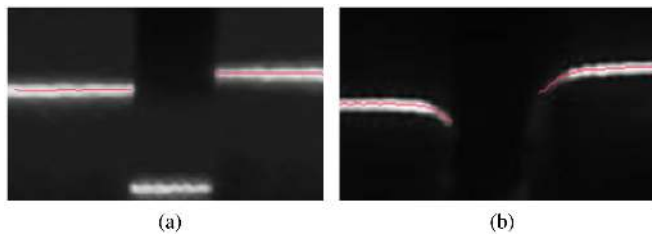

Fig. 8. Illustrating the CoMP algorithm. (a) On straight edge gap. (b) On curved edge gap.

then used to measure the G&F in a straightforward approach, as depicted in Fig. 9(a).

However, cars are designed with flowing panels and curved panels and rounded corners so that the two-points method cannot be applied. Due to the geometrical characteristics of the laser profile, the definition of G&F needs to be adjusted, as shown in Fig. 9(b). The circle fitting method in [4] needs a predefined radius to work correctly; hence, the curvature of the measured
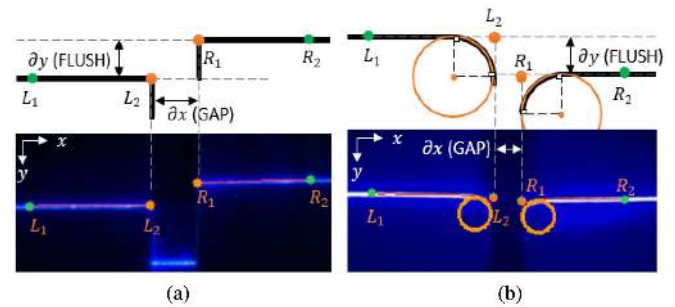
Fig. 9. Extreme points localization using: (a) the two-points method for flat edge gap; (b) the circle fitting method for curved edge gap.

object needs to be studied beforehand. This method is inconvenient. Instead, in this study, we devise an automatic curve fitting method to obtain the measurement points L_2 and R_1 without prior knowledge of the radius.

From analytic geometry, the circle passing through three non-collinear points $p_1(x_1, y_1)$, $p_2(x_2, y_2)$, and $p_3(x_3, y_3)$ is unique and can be found by solving the determinant equation

$$\begin{vmatrix} x^2 + y^2 & x & y & 1 \\ x_1^2 + y_1^2 & x_1 & y_1 & 1 \\ x_2^2 + y_2^2 & x_2 & y_2 & 1 \\ x_3^2 + y_3^2 & x_3 & y_3 & 1 \end{vmatrix} = 0. \quad (8)$$

To satisfy the requirement that the slopes of the line joining point p_2 and point p_3 and the line joining point p_1 and point p_2 must not be same

$$\frac{y_3 - y_2}{x_3 - x_2} \neq \frac{y_2 - y_1}{x_2 - x_1}. \quad (9)$$

Equation (8) can be solved by evaluating the cofactors M_{1x} for the first row of the determinant. The determinant can be written as an equation of these cofactors

$$(x^2 + y^2)M_{11} - xM_{12} + yM_{13} - M_{14} = 0. \quad (10)$$

Because $(x^2 + y^2) = r^2$, (10) can be simplified to

$$r^2 - x\frac{M_{12}}{M_{11}} + y\frac{M_{13}}{M_{11}} - \frac{M_{14}}{M_{11}} = 0. \quad (11)$$

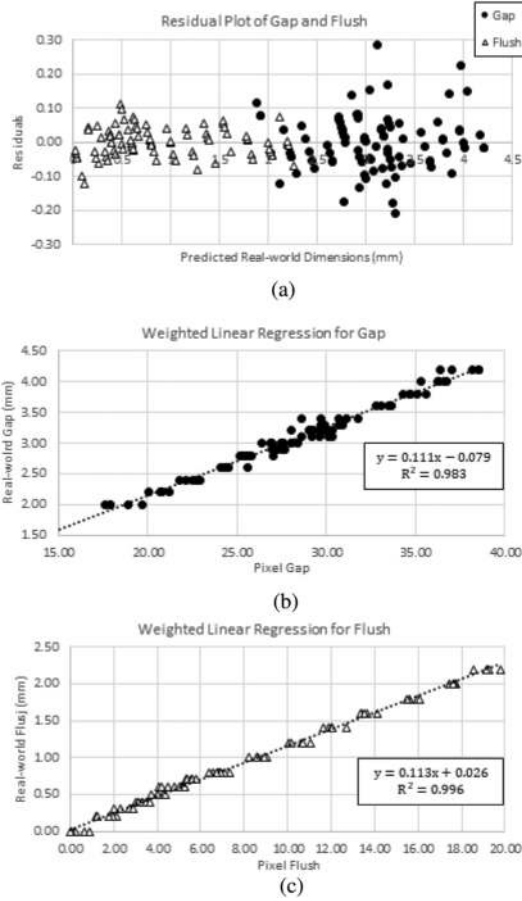Fig. 10. (a) Scatter plot for the residuals versus the real-world dimensions of G&F. (b) Plotting the weighted linear regression for gap. (c) Plotting the weighted linear regression for flush.

Algorithm 1: Extreme Points Localization Algorithm.

Input: Contour $C := \{C_L, C_R\}$
Result: Extreme points $\{L_2, R_1\}$
1) Initialize a vector of points in the contour C:
   $\{p_0, p_1, \ldots, p_n\}$
2) Evaluate the noncollinear criteria of all points using Equation (9)
   a) If all points are collinear and $|p_0(y) - p_N(y)| \le 3$:
      Extract $\{L_2, R_1\}$ using two-points method and go to step 5.
   b) If points are noncollinear and
      $|p_0(y) - p_N(y)| \ge 3$: go to step 3.
3) Loop through all points $\{p_0, p_1, ..., p_N\}$ to determine the best fitted circle:
   $c_i = \text{argmax}_{i,k}(\beta(c_i(k)))$
   with:
   - $c_i(k) = Circle(p_{i-k}, p_i, p_{i+k})$ using Equation (13)
   - $\beta(c_i) = \frac{\sum_{h=1}^{N(c_i)} E(p_h)}{N(c_i)}$
   - $E(p_h) = \begin{cases} 1, & \text{if the pixel point } p_h \in c_i \wedge p_h \in C \\ 0, & \text{otherwise} \end{cases}$
   where $\beta(\bullet)$ is the circle factor, $N(c_i)$ is the total number of points on the circle c_i, and
   $k = [1, N-1]$.
4) Readjust end point using the fitted circle c_i
   a) $B = boundingBox(c_i)$
   b) For C_L: L_2 is the top right corner of B
   c) For C_R: R_1 is the top left corner of B
5) Obtain a pair of measuring points: $\{L_2, R_1\}$

Additionally, the general equation of a circle with radius r_0 and center (x_0, y_0) is

$$(x - x_0)^2 + (y - y_0)^2 - r_0^2 = 0$$
$$\Leftrightarrow r^2 - 2xx_0 - 2yy_0 + x_0^2 + y_0^2 - r_0^2 = 0. \quad (12)$$

From Equations (11) and (12), we can solve for the radius r_0 and center (x_0, y_0) of the fitted circle as

$$x_0 = 0.5 \frac{M_{12}}{M_{11}}; y_0 = -0.5 \frac{M_{13}}{M_{11}}$$

$$r_0 = x_0^2 + y_0^2 + \frac{M_{14}}{M_{11}}. \quad (13)$$

Algorithm 1 shows the sequence needed to implement the extreme points localization algorithm. The same process is performed for both Ct_L and Ct_R contour. Examples of the extracted extreme points can be shown in Figs. 9 and 11(d).

E. G&F Measurement

1) Gap & Flush Measurement: The G&F measurement is done by determining the right-hand side of the equation

$$\mathbf{m} = \mathbf{MB} \quad (14)$$

where $\mathbf{m}$ is the measurement in standard units (mm), $\mathbf{M}$ is the measurement in pixels, and $\mathbf{B}$ is the pixel resolution for G&F measurement. $\mathbf{M}$ can be obtained following the reverse triangulation principle presented in Fig. 3(a). The measurements in pixel $\mathbf{M}$ of G&F can be calculated as

$$\mathbf{M} = \begin{bmatrix} G \\ F \end{bmatrix} = \begin{bmatrix} \partial X \\ \partial Z \end{bmatrix} = \begin{bmatrix} 1 & 0 \\ 0 & 1/\tan\alpha \end{bmatrix} \begin{bmatrix} \partial x \\ \partial y \end{bmatrix} \quad (15)$$

where ∂Z is the height difference (i.e., flush) and ∂X is the horizontal difference between the two panels (i.e., gap). As shown in Fig. 9, ∂y is the normal distance between the point R_1 on the right panel with the reference line constructed from points L_1 and L_2 on the left panel

$$\partial y = \frac{|(x_{L_2} - x_{L_1})(y_{L_1} - y_{R_1}) - (x_{L_1} - x_{R_1})(y_{L_2} - y_{L_1})|}{\sqrt{(x_{L_2} - x_{L_1})^2 + (y_{L_2} - y_{L_1})^2}}. \quad (16)$$

The horizontal distance ∂x can be inferred by using the Pythagorean equation and the distance between two extreme points L_2 and R_1

$$\partial x = \sqrt{(x_{L_2} - x_{R_1})^2 + (y_{L_2} - y_{R_1})^2 - \partial y^2}. \quad (17)$$
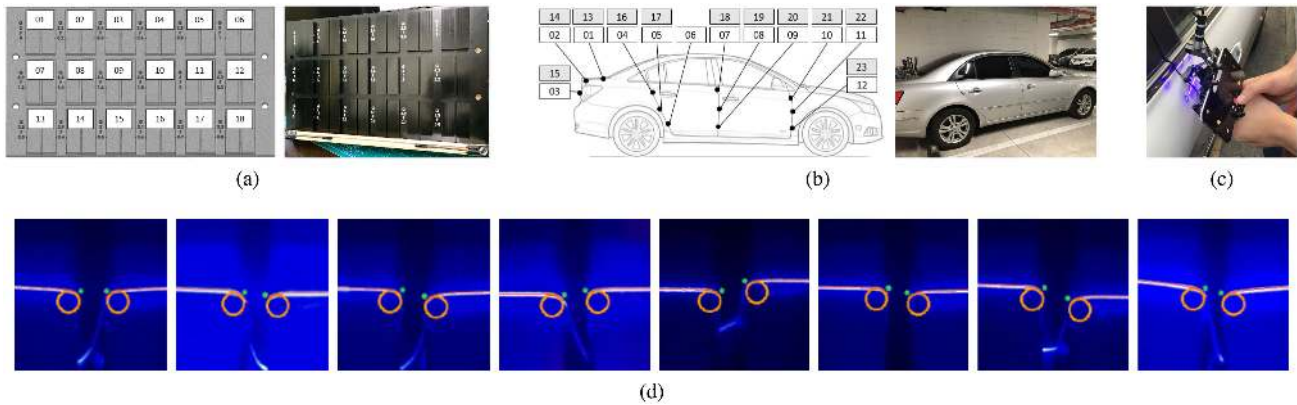
Fig. 11. Experimental procedure. (a) Reference standard. (b) Measuring spots on real car: white boxes are measuring point on the car's right side while gray boxes are measuring points on the car's left side. (c) Using the SLM device in contact operation mode. (d) Examples of extreme points localization using circle fitting approach for curved panels and rounded corners.

TABLE III
OPTIMUM POLYNOMIAL ORDER ANALYSIS

Polynomial	GAP		FLUSH	
order, m	$S_r(m)$	$S_r(m)$/(n-m-1)	$S_r(m)$	$S_r(m)$/(n-m-1)
1	0.6232	**0.0071**	0.1501	**0.0017**
2	0.6634	0.0076	0.1497	0.0017
3	0.6996	0.0081	0.1467	0.0017

From (15) and (18), the G&F measurement can be obtained using (14). Finally, the measured results and laser profiles are displayed on the smartphone screen, signaling one completed measurement.

2) Calibration: To complete the right-hand side of (14), the pixel-to-real-world conversion coefficients $\mathbf{B} = [B_g, B_f]$ are needed. A direct calibration method was performed on a standard reference with 18 known G&F values [see Fig. 11(a)]. The gap value has a range of 2.0–4.2 mm, and the flush value has a range of 0.0–2.2 mm. These two ranges satisfy the requirements stated in Section II. The SLM device was used to measure each G&F point five times, and the obtained data are plotted against the pixel dimensions, as shown in Fig. 10. We modeled the relationship between the pixel and real-world dimensions using the polynomial regression method.

First, we determine the optimum order of the polynomial model by calculating the variance defined as $S_r(m)/(n - m - 1)$, where n is the number of data points, $S_r(m)$ is the sum of the square of residuals, and m is the order of the polynomial. The optimum order is considered as to be the one where the variance is minimum or where there is no significant decrease in its value as the degree of polynomial is increased. From the variances in Table III, we choose the first-order polynomial.

Second, ordinary linear regression is then applied on the data. The scatter plot for the residuals versus the predicted real-world G&F dimensions is shown in Fig. 10(a). This chart shows evidence that the variances are not constant. In situations like this, it may not be reasonable to assume that every observation should be treated equally, hence, weighted

least square is used to maximize the efficiency of parameter estimation

$$B_g = (G^T W_g G)^{-1} G^T W_g g$$
$$B_f = (F^T W_f F)^{-1} F^T W_f f \tag{18}$$

where g and f are the real-world G&F dimensions, G and T are the pixel G&F dimensions obtained from the extreme point localization algorithm, W_g and W_f are the weighted matrices, and B_g and B_f are the polynomial coefficients. The coefficients B_g and B_f were estimated using an open-source statistics tool [19] and are plotted in Fig. 10(b) and (c). The weighted linear regression models show a good fit to the data and have the R^2 values of 0.983 for gap and 0.996 for flush, respectively. After that, B_g and B_f are stored in the database for later uses. Notice that since the smartphone can be removed from the triangulation structure, the SLM device is checked with the reference standard before each measurement session to compensate for the offset created when reattaching the smartphone to the SLM device. More details are discussed in Section IV-A.

IV. EXPERIMENTS AND DISCUSSION

A. Uncertainty Evaluation

The experimental setup consists of two sets of reference standard as shown in Fig. 11(a). Each set includes 18 points with known G&F dimensions. The reference standards were manufactured precisely using black anodized aluminum. In the experimental procedure, one set was used as the calibration standard and one was used as the test target. The same measuring routine was performed on both the calibration standard and the test target. The experiments were performed under laboratory conditions with stable illumination conditions.

The measurement uncertainty of the SLM device must be quantified and considered in order to demonstrate conformance with specifications. The experimental procedure followed the methodology for evaluation of measurement uncertainty industrial measurement [20]. This method utilizes the practical tools

TABLE IV
RESULTS FROM MEASUREMENT OF THE CALIBRATION STANDARD

Spot	GAP						FLUSH					
	Nominal	Mean	Standard Deviation	Standard Uncertainty	Offset	Relative Error	Nominal	Mean	Standard Deviation	Standard Uncertainty	Offset	Relative Error
	(mm)	(mm)	(mm)	(mm)	(mm)	(%)	(mm)	(mm)	(mm)	(mm)	(mm)	(%)
1	2.000	1.902	0.024	0.007	0.098	4.90	0.000	0.010	0.019	0.006	-0.010	0.00
2	2.200	2.314	0.029	0.009	-0.114	5.18	0.200	0.187	0.021	0.007	0.013	6.50
3	2.400	2.401	0.018	0.006	-0.001	0.04	0.400	0.378	0.024	0.008	0.022	5.50
4	2.600	2.584	0.037	0.012	0.016	0.62	0.600	0.564	0.032	0.010	0.036	6.00
5	2.800	2.887	0.033	0.010	-0.087	3.11	0.800	0.743	0.025	0.008	0.057	7.12
6	3.000	2.942	0.014	0.004	0.058	1.93	1.000	0.979	0.027	0.009	0.021	2.10
7	3.200	3.241	0.051	0.016	-0.041	1.28	1.200	1.215	0.019	0.006	-0.015	1.25
8	3.400	3.372	0.037	0.012	0.028	0.82	1.400	1.389	0.028	0.009	0.011	0.79
9	3.600	3.523	0.017	0.005	0.077	2.14	1.600	1.617	0.021	0.007	-0.017	1.06
10	3.800	3.726	0.022	0.007	0.074	1.95	1.800	1.801	0.027	0.009	-0.001	0.06
11	4.000	3.968	0.020	0.006	0.032	0.80	2.000	2.047	0.032	0.010	-0.047	2.35
12	4.200	4.103	0.022	0.007	0.097	2.31	2.200	2.200	0.033	0.010	0.000	0.00
13	2.800	2.750	0.013	0.004	0.050	1.79	0.300	0.330	0.017	0.005	-0.030	10.00
14	2.900	2.895	0.022	0.007	0.005	0.17	0.400	0.411	0.041	0.013	-0.011	2.75
15	3.000	2.958	0.036	0.011	0.042	1.40	0.500	0.493	0.014	0.004	0.007	1.40
16	3.100	3.140	0.031	0.010	-0.040	1.29	0.600	0.626	0.024	0.008	-0.026	4.33
17	3.200	3.162	0.016	0.005	0.038	1.19	0.700	0.717	0.024	0.007	-0.017	2.43
18	3.300	3.231	0.026	0.008	0.069	2.09	0.800	0.776	0.024	0.008	0.024	3.00
	Worst-case		0.051	0.016	Average	1.83%	Worst-case		0.041	0.013	Average	3.15%

of measurement systems analysis (AIAG's MSA [21]) to obtain the measuring process uncertainty (Type A), whereas defines other uncertainty sources following the GUM manual [22]. The combined uncertainty can be calculated from calibration uncertainty, repeatability and reproducibility uncertainty, and temperature uncertainty, as described in the following sections.

B. Calibration Uncertainty

Before beginning the measurement session, the SLM system needs to measure the calibration standard before being used on the test target. This gives the measurement traceability to primary standards. Each G&F point was measured ten times. The deviation of the measurements on the calibrated spots from the true values gives the calibration offset, as shown in Table IV. The uncertainty of the calibration process is determined by the worst-case value: 0.016 mm for gap and 0.013 mm for flush. In addition, each point were verified by measuring the same spots with a calibrated digital caliper (Mitutoyo model 500-151-20) and digital flush gauge. Both instruments have an uncertainty of 0.01 mm ($k = 2$ for a 95% confidence). Dividing by 2 gives the standard uncertainty of 0.005 mm ($k = 1$). The SLM device then inherits this uncertainty. The combined uncertainty for the whole calibration routine then becomes a component of uncertainty in Table VI.

C. Repeatability and Reproducibility Uncertainty

Repeatability is estimated by making a series of measurements, generally by the same person and under the same conditions, and then finding the standard deviation of these measurements. The repeatability captures uncertainty from random variation in the use of the device by the operator. Hence, it also includes uncertainty from alignment errors during repeated measurements, and, therefore, does not need to be evaluated as a separate component of uncertainty. Reproducibility is estimated by making a series of measurements, each by a different person.

One method of determining both repeatability and reproducibility in a single test is a Gage Repeatability and Reproducibility (Gage R&R) analysis of variance (ANOVA). In the Gage R&R study, 18 parts are measured by ten operators. In each measurement, the operator aligns the SLM device, acquires the measurement, and removes the device. Each point is measured ten times in a random order, for a total of 1800 acquisitions. The ANOVA statistical analysis is then used to quantify the variations in the results due to three sources: the actual component variation, the repeatability of the measurement system, and the reproducibility of results between different operators. The Gage R&R study was performed using the statistical software Minitab 18, and the results of this study are shown in Table V. The total Gage R&R standard deviations for gap are 0.064 mm and for flush is 0.045 mm, respectively. These values are then included in the uncertainty budget in Table VI.

D. Temperature Uncertainty

The temperature may affect measurements in terms of thermal expansion of the object being measured. The change in length of aluminum parts when exposed to different temperatures can introduce uncertainty into the measurement. According to the recommended indoor temperatures [23], the preferred temperature for exposures less than 3 h are 18.5 to 27 °C (when outside is 35 °C) and 17 to 22 °C (when outside is 21 °C). Hence, the maximum indoor temperature different is around 10 °C. The linear expansion coefficient of aluminum is 23 μm/m°C. One spot on the reference standard consists of two panels, each having a width of 0.02 m. Hence, applying the linear thermal expansion formula [23], the total width difference is around $2 \times (0.02 \times 23e^{-6} \times 10 \times 1000) = 0.009$ mm. The maximum height of the spot is 0.01 m, hence, the total height difference is around $2 \times (0.01 \times 23e^{-6} \times 10 \times 1000) = 0.005$ mm. The temperature uncertainty is included in the uncertainty budget using a rectangular distribution.

TABLE V
Gage R&R Study of the SLM Device

| | Reference Standard | | | | Real Car | | | |
| | GAP | | FLUSH | | GAP | | FLUSH | |
Source	StdDev (mm)	%Contribution	StdDev (mm)	%Contribution	StdDev (mm)	%Contribution	StdDev (mm)	%Contribution
Total Gage R&R	0.064	1.20	0.045	0.47	0.099	4.84	0.071	2.94
Repeatability	0.038	0.43	0.025	0.15	0.066	2.16	0.043	1.09
Reproducibility	0.051	0.77	0.037	0.33	0.073	2.68	0.057	1.85
Part-to-Part	0.584	98.80	0.650	99.53	0.438	95.16	0.411	97.06
Total Variation	0.587	100.00	0.652	100.00	0.449	100.00	0.417	100.00
Distinct Categories	12		20		6		8	

TABLE VI
G&F Uncertainty Budget for Reference Standard

GAP

Source of Uncertainty	Value	Probability Distribution	Divisor	Standard Uncertainty
Calibration uncertainty	0.017 mm	Normal	1	0.017 mm
Temperature	0.009 mm	Rectangular	$\sqrt{3}$	0.005 mm
Total Gage R&R	0.064 mm	Normal	1	0.064 mm
Combined standard uncertainty				0.066 mm
Expanded uncertainty (k=2, 95% confidence)				**0.133 mm**

FLUSH

Source of Uncertainty	Value	Probability Distribution	Divisor	Standard Uncertainty
Calibration uncertainty	0.014 mm	Normal	1	0.014 mm
Temperature	0.005 mm	Rectangular	$\sqrt{3}$	0.003 mm
Total Gage R&R	0.045 mm	Normal	1	0.045 mm
Combined standard uncertainty				0.045 mm
Expanded uncertainty (k=2, 95% confidence)				**0.094 mm**

TABLE VII
G&F Uncertainty Budget for Real Car

GAP

Source of Uncertainty	Value	Probability Distribution	Divisor	Standard Uncertainty
Calibration uncertainty	0.017 mm	Normal	1	0.017 mm
Temperature	0.009 mm	Rectangular	$\sqrt{3}$	0.005 mm
Total Gage R&R	0.099 mm	Normal	1	0.099 mm
Combined standard uncertainty				0.100 mm
Expanded uncertainty (k=2, 95% confidence)				**0.201 mm**

FLUSH

Source of Uncertainty	Value	Probability Distribution	Divisor	Standard Uncertainty
Calibration uncertainty	0.014 mm	Normal	1	0.014 mm
Temperature	0.005 mm	Rectangular	$\sqrt{3}$	0.003 mm
Total Gage R&R	0.075 mm	Normal	1	0.075 mm
Combined standard uncertainty				0.077 mm
Expanded uncertainty (k=2, 95% confidence)				**0.154 mm**

E. Expanded Uncertainty

The reported combined uncertainty of the measurements is determined by summing in quadrature as stated in GUM [22], yielding values of 0.076 mm for gap and 0.045 mm for flush. Therefore, the expanded uncertainty at a 95% confidence interval, which is given by multiplying the standard error by $k = 2$, is 0.133 mm for gap and 0.094 mm for flush.

F. Real Car Evaluation

A second experiment was set up on a real car to assess the real-world application of the SML device. The experiment took place in our lab's indoor parking garage [in Fig. 11(b)], where the lighting closely resembles the real factory conditions.

The same measurement routine was performed as in Section IV-A. Before each spot was measured, the SLM device was used to check with the calibration standard. A total of 12 spots on the car body were selected for testing. Each spot's nominal values of G&F were first validated by the calibrated digital caliper and digital flush gauge, at 0.01 mm uncertainty. Then, three operators measured each part ten times in a random order. The operator aligned the SLM device, took the measurement, and removed it afterward. The results of the Gage R&R study using ANOVA for the measurement process are shown in Table V. The total Gage R&R standard deviation is included in the uncertainty budget, as shown in Table VII.

The temperature range is assumed to be similar to the one defined in Section IV-A, where the maximum temperature different is around 10 °C. We assume the temperature uncertainty is similar to the reference standard defined in Section IV-A.
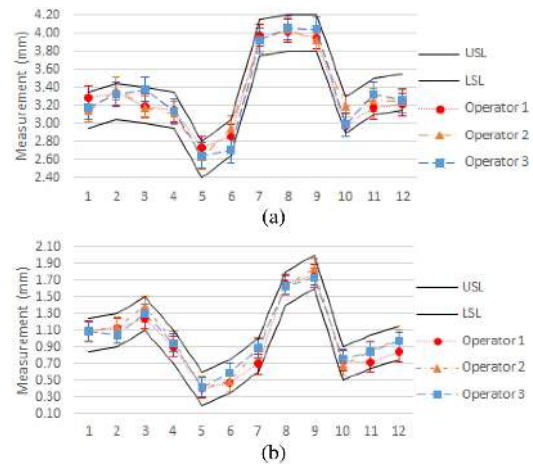

Fig. 12. Plotting the mean and standard uncertainty of measurements of each operator on real car. (a) Gap measurement. (b) Flush measurement.

Hence, the same temperature uncertainty (gap: 0.009 mm and flush: 0.005 mm) were added to the uncertainty budget.

The expanded uncertainty values in measurements of G&F on the real car were 0.201 and 0.154 mm, respectively. Also, as seen in Table V, variations between parts (Part-to-Part) account for most of the uncertainty in the measuring process (95.16% for gap and 97.05% for flush). Fig. 12 shows a plot of the mean and standard uncertainty values of measurements by each operator. As shown in the figures, all results fall clearly within the limits of the specifications stated in Section II.

Another critical feature to be highlighted is the extreme points localization for curved G&F measurements on a real car. The

Fig. 13. (a) Illustration of the hybrid contact/noncontact operation mode of the system described in [12]. (b) Real-world demonstration of using the device.

SLM application can automatically detect a curved edge and apply the appropriate extreme point extraction method. It was possible to analyze the image and extract the subpixel position of the extreme points with a high accuracy, as shown in Fig. 11(d).

G. Comparison With Other Methods

A comparison with the smart portable laser triangulation system [12] shows the competitive advantages of the SLM device. The device described in [12] comprises several hardware components: a 405-nm laser projector, a Raspberry Pi Zero, a Raspberry PiCam, a ToF laser module, and a smartphone. In this system, the Raspberry Pi manages data acquisition and processing, whereas the smartphone acts as the middleware for exchange of data with the production line and powers the whole system. The ToF sensor is used to switch ON/OFF the laser source when the device-to-target distance exceeds the functioning range (around 30–40 mm). The operator needs to align the device to the target surface as shown in Fig. 13. Hence, this device operates in the contact measurement mode.

Meanwhile, the proposed SLM device also uses a 405-nm laser projector. However, it uses a smartphone as both the image acquisition device and the processing unit. The measurement data are stored inside the smartphone's and can be exchanged with the plant middleware through Wifi communication. The SLM device works in a contact mode in which stand-off supports are used. Based on feedback from experiments, this helps in improving the ease of use and also lowering the uncertainty associated with operators. The Type A uncertainty of our SLM device on a real car is $0.099 \times 2 = 0.19$ mm for gap and $0.077 \times 2 = 0.15$ mm for flush (at 95% confidence interval). These values are lower than the values reported in [12] (0.38 mm for gap and 0.33 mm for flush at 95% confidence interval). Hence, in terms of measurement performance, the proposed SLM device is clearly more stable. In addition, the SLM device is more accurate than manual measuring methods, which are highly reliant on operator skills.

For a better quantification of the improvement in productivity of the SLM device, Table VIII shows the average time for performing each measurement task. The SLM device significantly reduces the cycle time per point measured. Subsequently, the man-hours required to measure a whole car can be reduced by 1.38 h compared to the manual method being used currently. Also, the measurement data are stored digitally in the device and can be transferred to the computer for reporting tasks. Unfortunately, we could not find any estimation of the processing time of the device in [12]. Therefore, we could not establish any comparison.

TABLE VIII
PRODUCTIVITY ANALYSIS

Measurement data	
Number of points/car	24
Number of measurements/point	10
Manual method (digital caliper & digital flush gauge)	
Device needed	2
People needed	2
Type A uncertainty (mm)	
Gap (mm)	0.20
Flush (mm)	0.18
Cycle time/point (s)	109.13
Manhour (MH)/point (s)	218.26
Manhour (MH)/car (h)	1.46
Portable device [12]	
Device needed	1
People needed	1
Type A uncertainty (mm)	
Gap (mm)	0.38
Flush (mm)	0.33
SLM device	
Device needed	1
People needed	1
Type A uncertainty (mm)	
Gap (mm)	0.19
Flush (mm)	0.15
Cycle time/point (s)	11.01
Manhour (MH)/point (s)	11.01
Manhour (MH)/car (h)	0.07
Saving of Manhour (MH)/car (h)	1.38

V. Conclusion

A smartphone-based laser triangulation device exploiting optical laser triangulation to assess G&F on a car body was presented in this article. The device combined a smartphone and a 405-nm laser line projector to guarantee the reliability of the measurement. According to the methodology, a sequence of images was processed by the laser extraction algorithm to detect the laser profiles. The algorithm outputted a new binary image that was passed to the feature point selection algorithm to identify the correct extreme points. With these pixel positions, the G&F measurement algorithm estimated the number of pixels in the cross section and outputted the G&F dimensions. A statistical analysis demonstrated that the average error is small, demonstrating the accuracy of the measurement. Furthermore, the device presented in this article compares favorably to other methods in the literature. For the experiments in this article, a working prototype of an SLM device was made using an Apple iPhone X. However, implementation of other smartphone models is possible.

The main drawback of the proposed SLM device was the structure that holded the triangulation setup. As smartphone size varies considerably, the structure may need to be adjusted to compensate for the change in dimensions. A more flexible and convenient structure that could accommodate different smartphone dimensions was needed. Additionally, tests were performed in an outdoor environment where the illumination was saturated by strong ambient light. The tests concluded that the system does not work in outdoor cases, which is another drawback of the SLM system.

References

[1] S.-H. Lee, C.-H. Jun, J. Jung, T.-S. Kim, and J.-H. Lee, "Identifying sources of dimensional variation affecting assembly quality of automobiles," in *Proc. 9th Asia Pacific Ind. Eng. Manage. Syst. Conf.*, 2008, pp. 753–759.

[2] D. Kosmopoulos and T. Varvarigou, "Automated inspection of gaps on the automobile production line through stereo vision and specular reflection," *Comput. Ind.*, vol. 46, no. 1, pp. 49–63, 2001.

[3] S. Kumar, P. K. Tiwari, and S. B. Chaudhury, "An optical triangulation method for non-contact profile measurement," in *Proc. IEEE Int. Conf. Ind. Technol.*, 2006, pp. 2878–2883.

[4] T.-T. Tran and C. Ha, "Non-contact gap and flush measurement using monocular structured multi-line light vision for vehicle assembly," *Int. J. Control, Autom. Syst.*, vol. 16, no. 5, pp. 2432–2445, 2018.

[5] EZ Metrology, EZ3D: Quick, accurate and mobile measurement solution for gap, flush and deformation tests, EZ Metrology, Headquarter, Commerce Township, Michigan, USA, 2019. Accessed on: Dec. 23, 2019. [Online]. Available: https://www.ezmetrology.com/prod_3d.php

[6] T. Pribanic, T. Petkovic, M. Donlic, V. Angladon, and S. Gasparini, "3D structured light scanner on the smartphone," in *Int. Conf. Image Anal. Recognit.*, pp. 443–450, 2016.

[7] Third Dimension, GapGun Pro, Third Dimension, Bristol, United Kingdom, 2018. Accessed on: Dec. 23, 2019. [Online]. Available: https://www.third.com/products/product-range/gapgun-pro

[8] Linear Measurement Instruments Corporation, LaserGauge Systems: gap and flush automotive exterior, Linear Measurement Instruments Corporation, Michigan, USA, Nov. 2015. Accessed on: Dec. 23, 2019. [Online]. Available: https://www.lmicorporation.com/LaserGaugeSystems

[9] Cognex Corporation, In-sight laser profiler: an easy-to-use measurement system for inspecting and verifying product dimensions, Cognex Corporation Massachusetts, USA, 2018. Accessed on: Dec. 23, 2019. [Online]. Available: https://www.cognex.com/products/machine-vision/3d-laser-profilers/in-sight-laser-profiler

[10] R. Slossberg and A. W. R. Kimmel, "Freehand laser scanning using mobile phone," in *Proc. Brit. Mach. Vis. Conf.*, 2015, pp. 88.1–88.10.

[11] GO0DMan Project, "Deliverable d3.1: Quality inspection systems", GO0DMan Project, April 6, 2018. Accessed on: Dec. 23, 2019. [Online]. Available: http://go0dman-project.eu/wp-content/uploads/2016/10/GO0D-MAN-DeliverableD3.1.pdf

[12] E. Minnetti *et al.*, "Smart portable laser triangulation system for assessing gap and flush in car body assembly line," in *Proc. II Workshop Metrology Ind. 4.0 IoT*, Jun. 2019, pp. 49–53.

[13] Micro-Epsilon, "A comparison of blue and red laser triangulation sensors", Micro-Epsilon UK & Ireland Ltd., June 30, 2016. Accessed on: Dec. 23, 2019. [Online]. Available: https://www.micro-epsilon.co.uk/news/2016/UK_ME272-Comparison-of-blue-and-red-laser

[14] S. R. Teli, S. Zvanovec, and Z. Ghassemlooy, "The first tests of smartphone camera exposure effect on optical camera communication links," in *Proc. 15th Int. Conf. Telecommun. (ConTEL)*, 2019, pp. 1–6.

[15] M. A. Gungor and I. Karagoz, "The effects of the median filter with different window sizes for ultrasound image," in *Proc. 2nd IEEE Int. Conf. Comput. Commun.*, 2017, pp. 549–552.

[16] E. P. Simoncelli, H. R. Sheikh, A. C. Bovik, and Z. Wang, "Image quality assessment: From error visibility to structural similarity," *IEEE Trans. Image Process.*, vol. 13, no. 4, pp. 600–612, Apr. 2004.

[17] D. K. Naidu and R. B. Fisher, "A comparative analysis of algorithms for determining the peak position of a stripe to sub-pixel accuracy," in *Proc. Brit. Mach. Vis. Conf.*, 1991, pp. 28.1–28.9.

[18] S. Suzuki and K. Abe, "Topological structural analysis of digitized binary images by border following," *Comput. Vis., Graph. Image Process.*, vol. 46, pp. 32–46, 1985.

[19] C. Zaiontz, Real Statistic Release 6.4, July 5, 2019. Accessed on: Dec. 23, 2019. [Online]. Available: http://www.real-statistics.com/real-statistics-release-6-4/

[20] J. E. Muelaner, A. Francis, M. Chappell, and P. G. Maropoulos, "A hybrid measurement systems analysis and uncertainty of measurement approach for industrial measurement in the light controlled factory," in *Conf. Sustain. Des. Manufacture*, 2015, pp. 1–12.

[21] *Measurement System Analysis*, 4th ed. Automotive Industry Action Group, 2010.

[22] Joint Committee for Guides in Metrology, "JCGM 100: Evaluation of measurement data—guide to the expression of uncertainty in measurement," Tech. Rep., JCGM, 2008.

[23] Engineering ToolBox, (2001). Accessed on: Dec. 23, 2019. [Online]. Available: https://www.engineeringtoolbox.com/

Long Hoang Pham received the B.S. degree in computer science and the M.S. degree in information technology management from International University, Ho Chi Minh City, Vietnam, in 2013 and 2017, respectively. He is currently working toward the Ph.D. degree in electrical and computer engineering with Sungkyunkwan University, Suwon, South Korea.

His current research interests include computer vision, image processing, and deep learning.

Duong Nguyen-Ngoc Tran received the B.S. degree in computer science and the M.S. degree in information technology management from International University, Ho Chi Minh City, Vietnam, in 2014 and 2018, respectively. He is currently working toward the Ph.D. degree in electrical and computer engineering with Sungkyunkwan University, Suwon, South Korea.

His current research interests include computer vision, image processing, and deep learning.

Jin Young Byun received the B.S. degree in electrical and information engineering from the Seoul National University of Science and Technology, Seoul, South Korea, in 2014. She is currently working toward the Ph.D. degree in electrical and computer engineering with Sungkyunkwan University, Suwon, South Korea.

Her research interests include computer vision, image processing, stereo vision, machine learning, and system-on-chip.

Chul Hong Rhie received the B.S. degree in material science from Seoul National University, Seoul, South Korea, in 2005. He is currently working toward the M.S. and Ph.D. degrees in automotive engineering from Kookmin University, Seoul, South Korea.

From 2005, he lead the Advanced Die R&D Team for three years, the Advanced Body Manufacturing Team for ten years, and managed the Advanced Manufacturing CAE Team for two years with Hyundai, Seoul.

Jae Wook Jeon (Senior Member, IEEE) received the B.S. and M.S. degrees in electronics engineering from Seoul National University, Seoul, South Korea, in 1984 and 1986, respectively, and the Ph.D. degree in electrical engineering from Purdue University, West Lafayette, IN, USA, in 1990.

From 1990 to 1994, he was a Senior Researcher with Samsung Electronics, Suwon, South Korea. Since 1994, he has been with Sungkyunkwan University, Suwon, where he was first an Assistant Professor with the School of Electrical and Computer Engineering and is currently a Professor with the School of Information and Communication Engineering. His research interests include robotics, embedded systems, and factory automation.